# A CT SCAN ANALYSIS WITH OPEN SOFTWARE OF THE EFFECT OF ORIENTATION AND CONFIGURATION OF FIBERS IN RANDOMLY ORIENTED FIBER COMPOSITES FAILURE

Lappeenranta–Lahti University of Technology LUT

Master's Programme in Mechanical engineering, Master's thesis

2025

Aapo Lehtinen

Examiners: Professor Timo Kärki

D.Sc. (Tech.) Marko Hyvärinen

ABSTRACT

Lappeenranta–Lahti University of Technology LUT

LUT School of Energy Systems

Mechanical Engineering

Aapo Lehtinen

**A CT scan analysis with open software of the effect of orientation and configuration of fibers in randomly oriented fiber composites failure**

Master's thesis

2025

47 pages, 21 figures and 4 tables

Examiners: Professor Timo Kärki and D.Sc. (Tech.) Marko Hyvärinen

Keywords: CT imaging, composite, failure mode, fiber orientation, numerical analysis, open software

CT scan data is analysed with open software and visually inspcted to explore fracture mechanics of short randomly-oriented glassfiber low-density polyethylene composite. It is revealed the method is not accurate enough to provide definite results that can be connected to tensile strength, but coincides with literature concluding fiber bundles and low-aspect ratio fibers have lower strength capacity than more thoroughly mixed and longer fibers. It is also apparent from the study that contrary to prior literature, randomly oriented fiber reinforced composites are not isotropic, but anisotropic. This is speculated to be caused by the extrusion and shearing of the composite mass during manufacturing. However it is also found against the consensus, that the samples break often where there is more fiber, instead of less.

TIIVISTELMÄ

Lappeenrannan–Lahden teknillinen yliopisto LUT

LUTin energiajärjestelmien tiedekunta

Konetekniikka

Aapo Lehtinen

**Kuitukomposiittimateriaalin TT kuvan analyysi avoimen lähdekoodin ohjelmistoilla selvitetyn kuitujen suuntiman ja asennon vaikutuksesta murtumamekanismeihin**

Konetekniikan diplomityö

2025

47 sivua, 21 kuvaa ja 4 taulukkoa

Tarkastajat: Professori Timo Kärki ja TkT Marko Hyvärinen

Avainsanat: TT-kuvaus, komposiitti, murtumismekaniikka, kuituorientaatio, numeerinen analyysi, avoin lähdekoodi

TT-kuvan data analysoidaan lyhyen satunnaisesti-suuntautuneen lasikuidun ja matalatiheyksisen polyeteenikomposiitin murtumamekaniikan tutkimusta varten avoimen lähdekoodin ohjelmistoilla. Selviää, että metodi ei ole tarpeeksi tarkka antaakseen täsmällisiä vetolujuuteen suhteutettavia tuloksia. Tulokset kuitenkin sivuavat paikoittain kirjallisuudessa todettuja asioita, kuten kuitunippujen ja matalan muotoosuhteen kuitujen alentavaa vaikutusta materiaalin vetolujuuteen, verrattuna paremmin sekoitettuun ja pitempään kuituun. Keskeisenä löytönä selviää myös, että ruiskumuovatussa komposiitissa kuidut eivät ole satunnaisessa järjestyksessä luoden isotrooppisen materiaalin, vaan järjestäytyvät suuntautuen ruiskun päädyn mukaisesti luoden anisotrooppisen materiaalin. Löytyy kuitenkin myös tietoa kirjallisuutta vastaan kuten se, että murtuma tapahtuu useimmiten kuituisemmassa kohdassa kappaletta.

ACKNOWLEDGEMENTS

Thank you to my friends who pressured me in to finishing this project and helped me through technical difficulties of word processing software. Also a special thanks to Eekhoff who wrote code I planned to use for computation of fibre orientation, diameter and segmentation, and his former professor Lake for replying to me within the day to provide me with code to use in my paper. Sadly it was left on the cutting room floor, due to time and skill restraints.

Aapo Lehtinen, 15.1.2025

# SYMBOLS AND ABBREVIATIONS

## Roman characters

| | | |
|---|---|---|
| A | Area | ($mm^2$) |
| $E_P$ | Energy of photons | (J) |
| $E_Y$ | Young's modulus | (MPa) |
| G | Shear modulus | (MPa) |
| l | Length | (mm) |
| P | Circumference | (mm) |
| r | Radius | (mm) |
| V | Volumetric fraction | (%) |
| z | Center length | (mm) |

## Greek characters

| | | |
|---|---|---|
| α | Angle | (°) |
| θ | Angle to normal plane | (°) |
| μ | Attenuation Coefficient | ($m^{-1}$) |
| ρ | Material density | ($kg/m^3$) |
| σ | Tensile stress | (MPa) |
| τ | Shear stress | (MPa) |

## Dimensionless quantities

| | |
|---|---|
| c | Circularity |
| p | Material property |

| | |
|---|---|
| $Z$ | Material atomic number |
| $\pi$ | Pi |

Abbreviations

| | |
|---|---|
| CT | X-ray Computed Tomography |
| FRC | Fiber-Reinforced Composite |
| GFRP | Glass-Fiber Reinforced Polymer |
| LDPE | Low-Density Polyethylene |
| ROFRC | Randomly Oriented Fiber-Reinforced Composite |

**Table of contents**

# 1 Introduction

Fiber-matrix composite use has seen a constant increase for a long time, especially the use of matrix glass-fiber reinforced polymers (GFRP) as a structural material has proliferated after the invention of faster production mechanisms of glass fibers in the 1930s. Now they are often the go-to choice for high strength and low weight applications like aeronautics, astronautics, nautical equipment and windmills. Because of the nature of the production, very large parts can be made with no fastening, unlike with aluminum for example. They have historically been troubled with the same issues as randomly oriented fiber reinforced composites (FRC) are now, which is trouble finding the focal failure points, understanding the varied failure mechanics and the unpredictable nature of the failures. Research in to the less utilized randomly oriented FRC materials that have been described as isotropic in prior literature, could provide insight and theories in to the fracturing mechanics of it. Short FRCs with randomly oriented fibers are not in widespread use as structural members in advanced mechanical fields, regardless of their relatively balanced multi-axial loading properties. This can be explained by the lack of understanding on the micro-damage mechanisms and the complexity of the internal microstructures, leading to unpredictable behavior. This is shown by the high Weibull modulus of composites, with large variance in material properties between samples. Research on how to make more predictable and improved material could make randomly oriented FRCs a competitor over the currently used structures and parts in ships, planes or even spacecraft. With possible weight savings and sustainable composites that have garnered a lot of attention recently like biocomposites, a more ecological option for the status quo could be found. A great tool to utilize in this matter is X-ray computed tomography (CT) imaging, which for composites has come a long way in the last couple decades and has provided ways of quantification for mechanical characteristics of materials. This has happened in particular for complex and heterogeneous materials, like composites. Partly this is because of the advancements made in the CT imaging resolution, contrast and input part size, but some of it can also be accounted by development of advanced algorithms that produce a solution domain from imaging data. It has been show to be useful in study of FRC breakage and fiber orientation and assessment when combined with numerical algorithms or even just visually. (Brunke, Stock, Stuart, Brockdorf, Drews, Müller, Donath, Herzen & Beckmann 2008, 1-2; Meyers

& Chawla 2008, 765 & 775-776; Stock 2008, 129-130; Reddy & Mandava 2013, 10-11; Hu, X.F., Chen, Tirvaudey, Tan & Tay 2016, 161; Hu, X., Fang, Xu, Dong, Xiao & Wang 2016, 1-2; Abhay, Sharma & Goyal 2018, 3711; Zhang, Feng, Bui, Hu & Yao 2020, 2; Karakoç, Miettinen, Virkajärvi & Joffe 2021, 1-2; Verho, Fortino, Hradil, Turpeinen, Immonen, Harlin & Sandquist 2022, 1-2.)

The goal of this research is to find a way to predict fracture mechanics and material strength of randomly oriented short FRC from CT imaging and show if commercially available CT imaging machines designed primarily for electronics inspection can be used to non-destructively acquire data from FRC materials for numerical analysis. All of this will be performed in the open source domain of code, with what time and money investment is expected of a master's thesis. Literature of the matter will be reviewed, followed by a method of imaging and data extraction. Data will be extracted and compared to literature, with a visual inspection of the images to confirm the data extraction accuracy.

## 1.1 Researched literature

Literature is researched in the following chapters to give an overview of the material, outline the known mechanics of composite material failure mechanics, and the usage of CT imaging for composites. Literature review will also be used in discussion of the mechanics. Literature was found mostly by google searching with mixed terms of CT x-ray imaging composites and biocomposites, industrial computed tomography, GFRP applications, short fiber reinforced composite fracture mechanics, or by searching above terms from LUT primo. Most of the research was from researchgate or sciencedirect/elsevier, and was accessed through sci-hub.se or its proxies. The ones that weren't found in sci-hub were accessed through LUT primo if available. Total amount of research used is 65 research papers, articles, conference papers or books.

## 1.2 Composites

Composites are defined as a mixture of 2 or more materials in a heterogeneous mixture, which have unique mechanical properties inherited from the material constituents. Usually composites are 2-part with either matrix-particle or matrix-fiber composition. Composites can be construed to have existed for as long as human history goes, beginning from crude

mud-matrix hay-fiber composites for building, to the current volumetrically dominant building material concrete made with with cement-matrix sand-particle constituents. Often in concrete more materials are added in to the mix like steel in the form of rebar or glass fibers, both to improve the relatively low tensile strength of concrete. In the modern world composites in mechanical engineering usually refer to polymer-matrix composites with fiber reinforcement. These are further divided in to thermoplastic polymers and thermosetting polymers, which nevertheless do the same function in the composite, but with different material characteristics. In these materials the fibers with the higher tensile strength and elastic modulus assume the load from the matrix. This transfer of force requires the interface of the matrix and fibers to withstand it, so the interfacial strength of the constituents is a core component of the properties of the composite material. The interface is a hotspot of activity, with multiple forces affecting its capabilities. First of these are chemical structures and bonds, including Van der waal forces, covalent bonds and acid-base interactions. The second is the physical forces in the structure, like frictional shear strength which can be separated from the chemical forces. (Moon, Lee, Cho & Kim 1992, 443; Zhandarov & Mäder 2005, 149-153; Meyers & Chawla 2008, 765-771.)

The most common fiber reinforcement in composites is glass fibers, usually combined with a thermoset epoxy polymer. These two have excellent fiber-matrix interface properties with proper pre-treatment of the fibers with silica, and their elastic modulus is relatively similar. A simple way to predict the properties of the composite from the constituents is by using a rule of mixtures known as the Voigt's average for axial loading, which goes (Meyers & Chawla 2008, 776):

$$p_c = p_f V_f + p_m V_m \tag{1}$$

Where $p_c$ is the material property of the composite, $p_f$ is the material property of the fiber, $p_m$ is the material property of the matrix, and $p_f$ and $p_m$ are the volumetric fractions of fiber and matrix respectively. This can be expanded in to upper and lower bounds of the material property, where the upper bound is the above mentioned Voigt's average and the lower bound comes from the inverse rule of mixtures known as the Reuss model, defined as (Meyers & Chawla 2008, 776):

$$p_c = \left(\frac{f}{p_f} + \frac{1-f}{p_m}\right)^{-1} \quad (2)$$

Where $f$ is the volume fraction of the fibers, and the rest are as above described. These attempt to define the properties of the composite in both perpendicular and axial directions. This is assuming the fibers are all parallel along an axis, which is not the case in randomly-oriented fiber reinforced composites (ROFRC). However it is accurate to some extent, though it has been surpassed in accuracy by modification (Blumentritt, Vu & Cooper 1974; Fu & Lauke 1998; Fu, Yue, Hu & Mai 2000; Junaedi, Baig, Dawood, Albahkali & Almajid 2021) or by other methods, like the bridging model (Huang, Zhang & Xue 2019), Halpin-Tsai's formulae(Affdl & Kardos 1976; Weber & Kamal 1992), Eshelby's equivalent inclusion method (Eshelby 1957; Chow 1977), the shear-lag model(Cox 1953; Piggott 1980), the Pan's method (Pan 1996) and finite element(FE)-method (Shokrian, Shelesh-Nezhad & Soudmand 2016; Grusev 2017).

The earliest of these, the shear-lag model is developed by Cox in 1953, it gives failure parameters of the fibers according to their orientation in the following formula from Hu et al. (2016, 3):

$$\tau_m = Q \sin h\,\eta\, z - \sigma \sin\alpha \cos\alpha \sin\theta \quad (3)$$

where (Hu et al. 2016, 3):

$$Q = \frac{H_m \zeta^2}{\eta^3 E_f \left(r_m - r_f\right) \cos h\,\eta\, l_f} \quad (4)$$

$$\eta = \sqrt{\frac{2 G_m}{E_f \left(r_m - r_f\right) r_f}} \quad (5)$$

$$\zeta = \sqrt{\frac{2 \sigma G_m \cos^2 \alpha}{E_a r_f \left(r_m - r_f\right)}} \quad (6)$$

$$r_m = r_f \sqrt{\frac{(1+v_f)}{v_f}} \tag{7}$$

In the above formulas 3-7, $E_{Ym}$ is the Young's modulus of the composite (MPa), $r_m$ is a radius for the fiber surrounding matrix (mm), $l_f$ half the length of the fibre (mm), $r_f$ is fiber radius (mm), $E_{Yf}$ is the Young's modulus for the fiber (MPa), $G_m$ is the shear modulus for the matrix (MPa), $\theta$ is the angle of the tensile forces to the fiber normal plane (°), $\alpha$ is the angle of orientation for the fiber(°), $\sigma$ is the stress applied (MPa) and finally $z$ is the length to the center of the fiber (mm). This analytical model from Hu et al. (2016) shows the pore formation at fiber ends that is explained in more detail in section 2.4.3.

Of these the bridging model is considered the most accurate, followed by the FE-method, followed by the Halpin-Tsai's method. Of these three, also iso-stress assemblage is a more accurate method than the iso-strain assemblage for higher fiber aspect ratios. For lower aspect ratios they're comparable (Huang et al. 2019, 11). For long fibers a layer-wise method has been suggested by Hashimoto, Okabe, Sasayama, Matsutani and Nishikawa (2012).

## 1.3 Randomly-oriented fiber reinforced composites

ROFRC are a type of composite in which the fibers are short and not aligned by any axis, plane or structure. They're mostly produced with extrusion or injection molding of parts, and are widely used in industries because they're easy to manufacture and have relatively good structural properties. Existing manufacturing tools are also highly compatible with the material, which cuts down on investment costs. The issues with ROFRC are mostly from the lack of predictability of fracture mechanics, making them highly uncertain in strength and elasticity. Another aspect of ROFRC is that during different flows their alignment is changed, and most manufacturing techniques used heavily lean on flow. Changes in the fiber orientation are also dependent on the shape of the fibers, mold and viscous behaviour of the composite melt. (Monfared 2020, 919 & 922-923; Patel & Jain 2021, 1-2.)

## 1.4 Natural fiber composites

A large amount of research has been made in to using natural fibers in composites because of their environmentally friendly status stemming from biodegradability, renewability (Faruk, Bledzki, Fink & Sain 2013, 1; Essabir, Bouhfid & Qaiss 2017, 147; Vijayakumar & Palanikumar 2020, 7915; Behera, Mohanty, Nath & Mahanta 2023, 1-2) and their affordability and safety for humans (Faruk et al. 2013, 3-5). They are not without caveat and the issues with them are their sensitivity to moisture, low strength and weak interfacial bonding, leading to diminished tensile strength, stiffness and impact strength of the composite. Compared to artificial fibers that are high strength, high molecular mass and hydrophobic character, the longevity and usability of the natural fiber composites is negatively affected by these traits. These materials are however very suited to replace typical polymer materials in places where material strength isn't critical and moisture isn't too prevalent, like car dashboards and indoor furniture. It should be kept in mind in applications like that some surface coating might be required, because of the lacking tribological qualities of the natural fibers. The interface strength can also be improved by treatment of the fibers with alkalis for example, known as mercerization. This replaces the hydroxyl groups in the fiber structure with sodium ions, improving its chemical bonding with matrixes. Another way of improving the interfacial strength is with mechanically making the fiber surface smoother. (Patel & Jain 2020, 1, 6; Putra, Budiman, Sambegoro, Santosa, Mahyuddin, Kishimoto & Inaba 2020, 8-11; Bhat, Kumar & Mural 2023 1-2.)

## 1.5 The failure mechanics of composites

The failure mechanics of fiber-reinforced composites (FRC) are well known and documented. The anisotropy and heterogeneity of FRCs cause relatively multifaceted micro- and macro-mechanical failure behavior (Scott, Sinclair, Spearing, Mavrogordato & Hepples 2014, 1; Hu, X., et al. 2016, 1-2; Hanhan, Agyei, Xiao & Sangid 2020, 1; Zhang et al. 2020, 2). Strained composites with parallel fibers go through 4 stages in their stress-strain curve. The stages are elastic deformation of both fibers and matrix, elastic deformation of fibers, but plastic deformation of the matrix, and lastly before fracture, the plastic deformation of both. The fourth stage is the fracture of fibers and the following fracture of the composite material (Goh, Aspden & Hukins 2004, 1092). This last step

described by Goh et al. (2004, 1092) isn't necessarily always the case, as the second to last stage can generally they can be divided in to two failure modes, of which the prior follows the stages aforementioned. One is the planar break of the fibers and soft matrix failure across the a failure plane. This is the primary mode of failure in composites with high volumetric fractions of strong, brittle and long fibers. In the other failure mode, the matrix fails to distribute the load to the fibers. This failure mode occurs when the adhesion between the fibers and matrix isn't strong enough, and the fibers are pulled out of the composite. This results in a nonplanar surface of failure. It is usually the result of short and thick fibers, or improperly pretreated fiber, which results in small pullout force and lower composite strength. Usually failures include these both modes of failure, and the amount of fiber failure and interface debonding also depends on the elastic mismatch of the fiber and matrix. (Williams 1990, 209-213; Moon et al. 1992, 444-446; Zhandarov & Mäder 2005, 157; Meyers & Chawla 2008, 794-799.)

Failures of composites are a collection of microscopic failures within the material. Other types of failure mechanics are delamination and shear-driven fracture, which are both related to laminated or layered composites, which are not relevant to this study. There are multiple methods suggested in research for numerical modeling the failure mechanics of composite materials. Some use phase field models and cohesive elements, some use 3D FE-analysis, and even a novel element-failure method has been suggested by Koyanagi, Kawamoto, Higuchi, Tan, and Tay (2021).

### 1.5.1 Analytical modelling of randomly oriented fiber composite failure mechanics

Analytical modelling of composite failure mechanics is a difficult task to perform, since the heterogeneous nature of the composite combined with the anisotropic nature of randomly oriented fiber composites gives a large scale of unpredictable failure points and theories, which can include combinations that supplement each other (Williams 1990, 209-210). However in all its simplicity the Voigt's average and Reuss model mentioned in section 2.1 can be used to predict material properties of these composites. It has shown use in case average fiber orientation of the ROFRC is known, with the caveat of being relatively inaccurate, especially with low fiber aspect ratios. (Mirkhalaf, Eggels, Anantharanga, Larsson & Fagerström 2019, 5-6; Huang et al. 2019, 6) However usually because of the complexity of the ROFRC the analytical analysis is divided in to

subdivisions of failure that can more easily be managed, like interfacial debonding, failure of the fiber, or failure of the matrix.

Interface debonding is the most investigated and crucial of the phenomena, since the interface is a central functional descriptor of a composite material. Interface debonding is explained by many schematics and formulas, with most of them including shear stresses in the interface. Hsueh (1990, 3) for example defined the applied stress required for debonding to initiate as:

$$\sigma_d = -\tau_s \left( \frac{2/a\left[(1+v_m)(1+(b^2/a^2-1)(E_{Ym}/E_{Yf}))(b^2\ln(b/a)-(b^2-a^2)/2)\right]^{(1/2)}}{(b^2/a^2-1)(E_{Ym}/E_{Yf})\coth(\alpha t)+2/(\exp(\alpha t)-\exp(-\alpha t))} \right) (8)$$

Where $v$ and $E_Y$ are the Poisson ratio and Youngs modulus, denoted as $m$ or $f$ as in matrix or fiber respectively. $\alpha$ comes from an equation also described by Hsueh (1990, 3):

$$\alpha = \frac{1}{a}\left[\frac{a^2 E_{Yf}+(b^2-a^2)E_{Ym}}{E_{Yf}(1+v_m)(b^2\ln(b/2)-(b^2-a^2)/2)}\right]^{(1/2)} \quad (9)$$

These equations get their physical dimensions from figure 1.

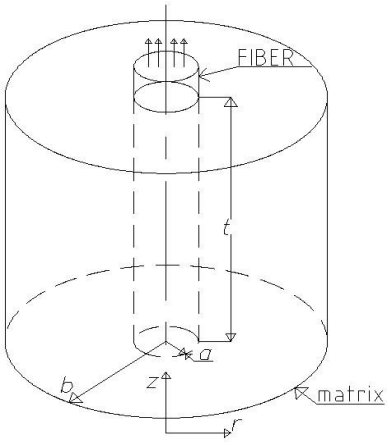


Figure 1. Drawing of the pull-out test.

However this doesn't directly take in to account the shear stresses caused by the low elastic modulus matrix being stretched around the high-elastic modulus fiber, as shown by Monfared (2020, 923-925).

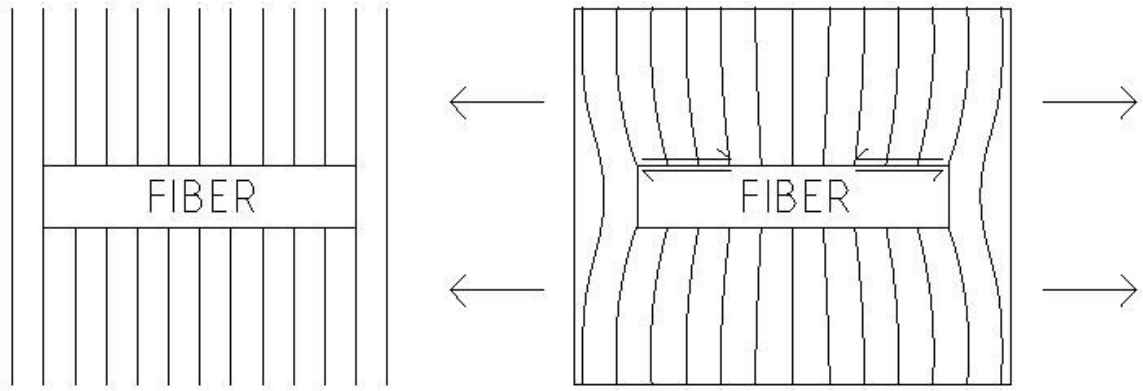


Figure 2. Shear stresses from the elastic mismatch of the matrix and fiber.

This phenomenon has been tackled analytically in literature and is numerically shown to exist and be quantifyable, especially in cases where fiber tips meet. (Hu, X. et al. 2016, 3-5; Hanhan et al. 2020, 5.)

### 1.5.2 Computer modelling of ROFRC failure mechanics

The most common method of numerical structural analysis is currently the FE-analysis. Its basic concept is dividing the geometry in to separate domains, known as a mesh. This mesh has nodes, from which through partial differential equations are formed through and solved with computers. The results can then be analyzed and the implications interpreted for the analyzed area, it's particularly good at assessing complex geometries like ROFRCs. However because of the random structure of the ROFRCs, input to the FE-analysis must be acquired from a non-destructive method like CT-imaging.

The FE-method has been applied for example in a studies by Pan (2008), Gusev (2017) and by Hanhan et al. (2020). Hanhans FE-method combined with an in-situ CT-image of the specimen showed, that when the hydrostatic stresses of the matrix is computed with (Hanhan 2020, 3):

$$\sigma_{hyd} = \frac{\sigma_{xx} + \sigma_{yy} + \sigma_{zz}}{3} \quad (10)$$

It shows a normal distribution within the matrix, with some elements showing higher stress locations, but only the larger groups were included to remove false positives from meshing. These larger groups were located at fiber tips in the hydrostatic hot-spots and correlated with the results from the CT-image, showing that FE-analysis of the hydrostatic stresses can be used to predict microvoid nucleation. It also shows that even though small fragments of fiber can be discounted in the calculations for the elastic properties of the composite, they affect the damage initiation and therefore strength of the composite.

A numerical phase field model in conjunction with a cohesive element model for progressive failure has also been developed for laminated composite materials by Zhang et al. (2020) It uses computational methods that are based on continuum damage mechanics and fracture mechanics, and attempts to model crack growth. It looks to be applicable to inspect crack penetration and deflection in ROFRC and even predicting crack patterns in transverse loading of the fibers.

Recently entropy has been used as the criterion for failure by Sato (2011), as with the polymer in the composite undergoes an irreversible damage internally, the molecular arrangement of the part changes, ultimately adding to the entropy. This method is a layered method used with the Mori-Tanaka theory. The entropy damage is derived from the stiffness of the matrix, which brings in to light the tensile strength and creep failures dependence on strain-rate. The Mori-Tanaka theory has been explored in a paper by Mori & Tanaka in 1973, where they separated the fibers as misfitting inclusions and calculated the strain of the matrix to come up with the average elastic energy in the matrix, appended by the locally fluctuating stress. Kagawa Umezu, Sakaue and Koyanagi (2023, 5) with this method used 3 different strain rates to approximate stress-strain curves for different fiber orientation angles from 5 degrees to 85 degrees, showing higher strength for axially orientated fibers as predicted. The averages of these with strain rates of 0.001/s 0.0001/s and 0.00001/s showed that different strain rates show different results, specifically higher strain shows higher ultimate tensile strength and total strain.

### 1.5.3 Outlier fiber head microvoid nucleation mechanics

Fiber outliers are defined as fibers in a FRC which tips are close to other fibers or in an orientation and location, which creates stress concentrations. Previous research has established with CT imaging that the failure mode of a tensile yielding glass reinforced polypropylene test subject and a thermoset epoxy resin matrix carbon fiber test subject was microvoid nucleation on tips of fibers often close to other fibers, especially outliers. (Hu, X. et al. 2016, 6; Hanhan et al. 2020, 5; Agyei & Sangid 2023, 1711-1712.)

A lot of other research has been made utilizing CT imaging on matrix-fiber composites, including the influence of voids on damage mechanisms in carbon/epoxy composites (Scott et al. 2014), and damage detection of carbon/epoxy laminates using synchrotron radiation CT (Scott et al. 2011). However these primarily focus on the fiber breakage or voids during production being the main failure condition or laminate composites characterized by aligned and regular reinforcements that don't have a lot of fiber outliers, ignoring the void generation from focal stress concentration locations at the fiber-matrix interface at fiber ends. This is related to the fiber-end aggregation-induced pore connection failure mechanic. Also studies have not inspected thoroughly the effect of fiber length or aspect ratio to this failure mode.

### 1.5.4 Fiber-end aggregation-induced pore connection mode

Generally not much CT imaging research has been made on biocomposite failure mechanisms, glass fiber epoxy matrix composites, or even randomly oriented short fiber reinforced composites. It was shown at least with carbon fibers in randomly oriented short FRC the defined cracking behaviors can be divided in to two classes. The fiber-end aggregation-induced pore connection mode, and the fiber-bridging crack mode. In these two modes of cracking behavior, in the first one the crack is connected through ends of fibers, connecting around the fibers. In the latter the crack advances through fibers, by either one of the prior explained modes of failure, either planar breaking of fibers or fiber pullout. It has been described that the fiber-end aggregation-induced pore connection failure mode was the prominent one in the randomly oriented short FRC. Fiber-bridging crack mode was is considered the primary failure mode in anisotropic unidirectional, multi-directional composites and longer fiber composites. (Hu, X. et al. 2016, 4-7.)

## 1.6 X-ray computed tomography

X-ray computed tomography is a non-destructive inspection technique where where a 3-dimensional voxel image can be created from a material. In the last decades CT imaging has advanced tremendously through advancement of sensors, and their clever use. Modern tools provides a way to detect fiber-matrix debonding because its possible to image constituents with similar attenuation coefficients in high resolution (Garcea, Wang & Withers 2018, 306-307, Zwanenburg, Norman, Qian, Kendall, Williams & Warnett 2023, 1-2). Because of the heterogeneity, anisotropy and the architecture of matrix-fiber composite, their failure behavior is dependent on the direction of load. 3D-imaging is especially helpful in pinpointing failure mechanisms. Even timelapses and imaging during testing is possible with CT. A flaw with CT imaging some materials is the difficulty of obtaining contrast and the price of the imaging tools. The contrast in CT imaging is based on the difference in linear attenuation coefficient of the three constituents. The constituents are fibers, matrix and damage or manufacturing defects. As written by Garcea et al. (2018, 306) the attenuation coefficient for any specific point can be defined as:

$$\mu(x,y,z) = K\rho\frac{Z^4}{E_p^3} \tag{11}$$

where $\rho$ is the material density (kg/m$^3$), $Z$ is the material atomic number, $K$ is a constant, and $E_p$ *(J)* is the energy of the directed photons. The contrast is therefore inherently better on some material combinations than others. This issue can be mitigated with utilizing methods like phase contrast, staining with a contrast agent or in the case of defects or damage, taking images of a loaded sample. The two main types of creating x-rays are an x-ray tube and a synchrotron. Of these two only the synchrotron creates monochromatic and coherent x-rays which in turn can create a more accurate image with higher contrast. X-ray tubes can only image with absorption of the x-rays, which limits the image quality and contrast, since they're affected by photonic phenomena like diffraction, refraction and interference. These cause unwanted background noise. Using these properties of photons it's possible to get higher quality images. This method is relatively unutilized in CT though

and only used in 2D imaging. (Mertens, Williams & Chawla 2014, 36-38; Garcea et al. 2018, 306-310; Kalasova, Brinek, Slouf, Duskova-Smrckova, Zikmund, Patakova & Kaiser 2020, 1; Margaritondo & Hwu 2021, 1-6; Gao, Hu, Xin & Sun 2022, 1-3.)

### 1.6.1 Post-processing of CT images

Analysing 3D-voxel images has been done in literature already with many computational algorithms, and many are openly available online under non-restrictive licences. ImageJ, ImageJ2 and its software fork Fiji have excellent tools for analysis. Especially Fiji contains libraries for analysis that are easy to install, update and utilize through a graphical user interface. It does lack in the performance side since it is coded in Java, and large images like in this study can just crash the analysis with some of the algorithms provided. It is suggested that images are condensed to not contain irrelevant data, and if possible only regions of interest are analysed.

A 3D computational algorithm to analyse fibre qualities like orientation, branching and diameter in image stacks is also proposed and provided by Eekhoff and Lake (2020). It's accuracy is tested with generated image stacks with known fibre populations. It's made in Matlab and C++ and requires the image stack and voxel dimensions for the stack. It does usually require some pre-processing since the background voxels need to be equal to zero and the images needs to be greyscale. The algorithm is an iterative one. The algorithm step by step performs 1) a pre-analysis which that determines local values for the voxel orientation and diameter estimates only analyzing every fourth voxel in all three dimensions, to reduce computational time. 2) Pre-analysis results are used as initial phase in the following full scale analysis. The analysis works with a spherical region being radially increased stepwise until objects are recognized, the pre-analysis results are then used to give an initial estimation on the solver equation. 3) After fiber properties are calculated the window increases until it finds surface objects enough to identify and call out the voxel as fiber end, intersection or a full fiber. 4) This is done until all objects in the image stack are recognized and their properties defined. Eekhoff and Lake concluded that the algorithm has a high accuracy for fibre diameter, branching and orientation analysis, with fibre orientation accuracy of within 1 deg, diameter calculations to be within 2% and intersections with a false positive rate of 0.1% and a false negative rate of 0.9%. It is

notable though that they estimate the accuracy to be dependant on the fiber diameter and image resolution ratio.

# 2 Materials and methods

Methods will include CT imaging of the fractured samples. The voxel models are analyzed through numerical means and literature is researched to confirm and hypothesize theory on fracture mechanics.

## 2.1 Materials

Our research had 3 samples, numbered 2, 7 and 9. All the samples were GFRP, with the constituent glass fibers being random lengths and the matrix being a low density polyethylene (LDPE). Samples are visible in figure 3.


Figure 3. Image of the torn GFRP samples.

The mixture is 20% glass fiber and 80% LDPE. The samples were produced with injection molding according to the specimen standard EN527-2/1BA/50 and tested according to the standard DIN EN ISO 527-1.

## 2.2 CT imaging

CT imaging will be performed on CT imaging machine from Waygate Technologies shown in figure 4, called the Phoenix Microme|x Neo.


Figure 4. Image of the CT-imaging machine.

It has maximum tube voltage of 160 kV / 20 W and maximum detail detectability of 0.5 µm with a max resolution of 2 µm. Maximum inspection area is 18” x 14” and the tube type is open microfocus.

### 2.2.1 Imaging setup and parameters

Subjects will be inserted in to the CT imaging machine shown in figure 5 after the tensile strength test. The samples were attached to the chuck, and imaged to the break plane from around 10mm away along the tensile stress test parallel axis. The sample will be turned in the chuck during imaging. This will leave circular imaging artifacts.

Figure 5. Image of the inside of the CT-imaging machine.

CT-imaging parameters are listed in table 1. It shows the differences between imaging for sample 2, which used a tube voltage of 60 kV and no filter. Samples 7 and 9 used a tube voltage of 120 kV and a 0,5mm copper filter.

Table 1. CT-imaging parameters.

| Sample | Tube Voltage | Tube Current | Exposure Time | Filter | Sensitivity | Averaging | Projections | Voxel Size |
|---|---|---|---|---|---|---|---|---|
| 2 | 60 kV | 60 µA | 1000ms | None | 4 | 4 | 1320 | 7,023 |
| 7 | 120 kV | | | 0,5 mm Cu | 2 | | | 7,232 |
| 9 | | | | | | | | 7,036 |

Sample 2 was imaged with a tube voltage of 60 kV, no filter and a sensitivity of 4. The rest of the parameters were the same as with samples 7 and 9. 7 and 9 used a tube voltage of 120 kV, Tube Current of 60 µA, exposure time of 1000ms, a 0.5mm Cu filter, sensitivity of 2, averaging of 4 and a total of 1320 projections. This ended up with sample 2 having a voxel size of 7,023 µm, sample 7 having 7,232 µm and 9 voxel size 7,037 µm.

## 2.3 Numerical analysis of CT voxel image

The voxel images will be published as a TIFF image stack. A thousand images for samples 7 and 9, and a 1582 images for sample 2. The fibers are analysed with programs under the MIT license called Fiji and Dhrishti. To turn the TIFF greyscale images in to a 3D model, the TIFF stack is imported in to Drishti import with 8-bit color scale, no subsampling and a voxel size of 7,023 micrometers. It will be exported as a .pvl.nc file, open source format voxel image. This voxel image format can be inspected visually for additional affirmation of analyses. Image stack can be resliced parallel to axis of the sample. In Fiji a threshold is set for the fiber, and the matrix. An auto threshold tool is used, provided in the Fiji toolset The algorithm for the threshold is an implementation of the Yen's thresholding method (1995). It was chosen because on visual inspection it seemed like the most accurate in this situation. It works through a multilevel algorithm (Chang 1995; Sankur 2004).

Before thresholding some imaging artifacts need to be suppressed in sample 7 and 9 by gating the maximum value of the brightness, this is done with the remove outliers tool, found in process → noise → remove outliers. 50 Pixels and a maximum value of 10000 suppresses the artifacts for better thresholding. Thresholding effects are shown in figures 6 and 7.

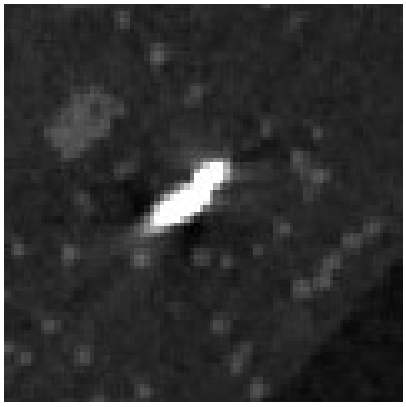

Figure 6. Artifacting pre-thresholding.

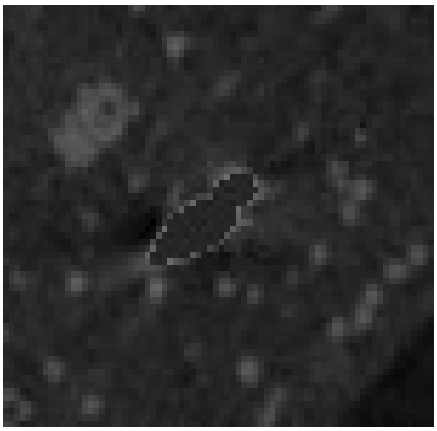

Figure 7. Artifacting post-thresholding.

Thresholding shows only the fibers in the matrix, and allows for analysis on the area amount of fiber and count of fibers. Contrast and brightness was increased for figures 6 and 7 for improved visibility.

### 2.3.1 Analysis of fiber orientation and count

In Fiji a particle analysis will be used to find out the approximate fiber count and orientation through each image layer. If a fiber passes through a layer in an angle, it will be imaged as an ellipse as shown in figure 8. A circularity definition of 0.00-0.96 will be defining a non x-axis oriented fiber, and circularity definition of 0.96-1.00 will be defining an x-axis oriented fiber. These values are derived from calculations below, in which the x-axis aligned fibers are +-45 degrees to the x-axis, and y-axis aligned fibers are over. A summary option is checked and the include holes setting is unchecked. Data is exported by saving the results as a csv file. A count of both types of fibers will be plotted, so the fiber count in the 2 orientations can be portrayed in conjunction with the plane of fracture. A visual inspection from plots will be concluded, outlier results will be dismissed, and trend lines will be formed with the LibreOffice Calc trendline tool from fiber counts between the beginning of proper imaging, and the fracture plane. For easier visualisation the plot for all samples will be centred approximately at the beginning of the fracture plane. The circularity formula used in particle analysis is defined in Fiji as:

$$c = \frac{4\pi \cdot A}{P^2} \tag{12}$$

Where $c$ is circularity, $A\ (mm^2)$ is the area, and $P\ (mm)$ is the circumference. The ellipse size is derived from simple trigonometry of the cross section of a round cylindrical fiber intersecting with a plane, as seen in figure 8 where $\alpha = 45°$.

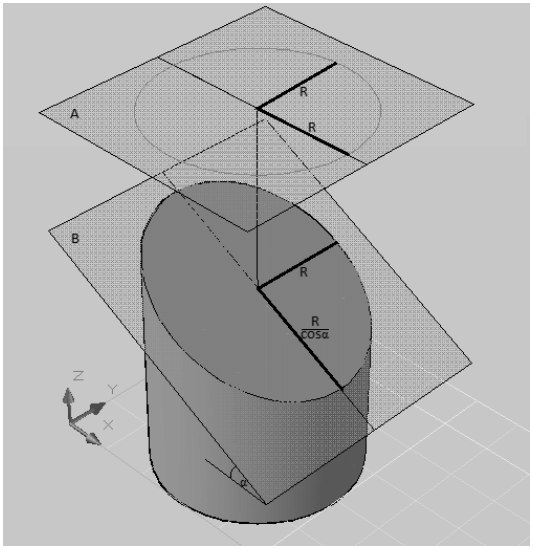


Figure 8. Elliptical area of a round fiber.

This comes out to:

$$a = \frac{r}{\cos\alpha} \tag{13}$$

The area $A$ of a circular or elliptical object is (Kivelä 1989, 32):

$$A = a\,r\,\pi \tag{14}$$

The perimeter $P$ of an ellipse is calculated by Ramanujans second approximation (Villarino 2005, 1):

$$P = \pi\,(a+b)\left(1+\frac{3h}{10+\sqrt{(4-3h)}}\right) \tag{15}$$

where (Villarino 2005, 1):

$$h = \left(\frac{a-b}{a+b}\right)^2 \tag{16}$$

The above formulas are added to formula 12, and the equation is solved, giving us the value $c \approx 0.96$.

The particle analysis counts and measures objects in the thresholded/binary images. It scans the image for an edge of an object, outlines it with the wand tool. After this its measured with the measure command, and filled to make invisible. Scanning then resumes to the end of the image. The caveats of this method of analysis is that it only divides the fibers in to two groups, closer to perpendicular to image plane and closer to parallel to image plane. It also has some misinterpretation modes, like with two or more fibers close to each-others being counted as elliptic, or a bundle of elliptic fibers counted as round. A higher resolution imaging setup would also be more accurate for this type of analysis, since the perimeter can change so much with a single pixel being added, so artifacts and impurities easily affect the fiber roundness. An example of how the analysis works for roundnesses 0.00-0.96, 0.50-1.00 and 0.00-0.50 can be seen in figures 9. 10. and 11. respectively.

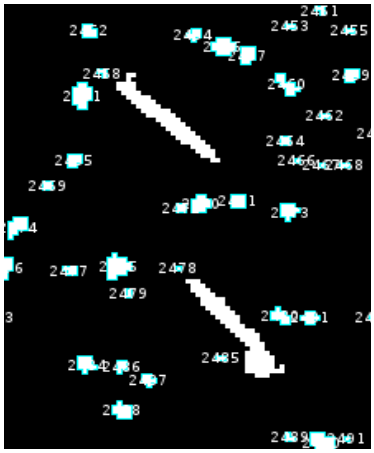

Figure 9. Roundness 0.00-0.50 in cyan outline.

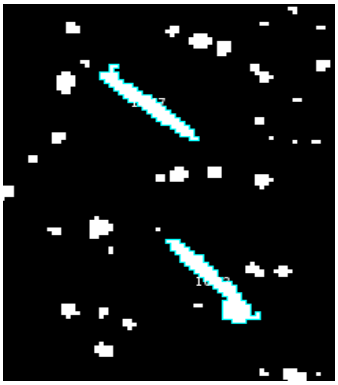

Figure 11. Roundness 0.50-1.00 in cyan outline.

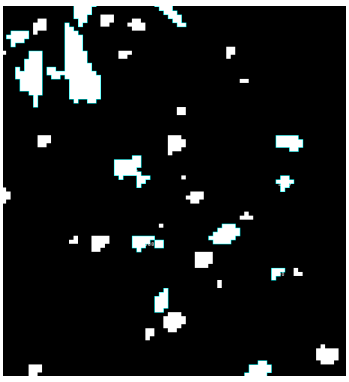

Figure 10. Roundness 0.00-0.96 in cyan outline.

To see the extremes, an analysis will be also performed to see the orientation of the 0.50-0.00 particles, which are aligned almost perpendicular to the x-axis.

## 2.4 Fiji analysis of area

In Fiji the same particle analysis also gives out total area of the objects in the image. This can be utilized to find out if the objects are in large clusters, or small single fibers. It also provides insight on the total fiber material at sections of the samples. Even though the samples are the same size and therefore the sample sections also should have the same area, it must be kept in mind since the imaging parameters and some preliminary processing have not been completely similar in the images, the images are not completely comparable to each other.

# 3 Results

Results are exported to csv files and analyzed with tools described in chapter 2 – Methods. Tables and graphs are used to interpret the results.

## 3.1 Fiber count data

The circularity was analysed and exported in to excel and some information was collected to table 2 from the data that is plotted in figure 12. The yield strength of the samples were yield_s2= 24.299, yield_s7= 24.569 and yield_s9 = 24.913 in MPa, as seen from table 2. That's a maximum difference of 2.496% in yield strength.

Table 2. Analysis results for 0.00-0.50 and 0.50-1.00 roundness.

| SAMPLE | SAMPLE 2 | SAMPLE 7 | SAMPLE 9 |
|---|---|---|---|
| YIELD STRENGTH (MPa) | 24.299 | 24.569 | 24.913 |
| (MIN)MAX FIBER COUNT ROUNDNESS 0.50-1.00 | (782)1032 | (972)1144 | (956)1489 |
| (MIN)MAX FIBER COUNT ELLIPTICAL 0.00-0.50 | (66)154 | (14)51 | (41)126 |
| ROUND FIBER TREND LINE ANGLE | -0.055747 | 0.021258 | 0.55937 |
| ELLIPTICAL FIBER TREND LINE ANGLE | 0.030038 | 0.018048 | 0.065098 |
| ROUND FIBER COUNT AVERAGE | 880 | 1070 | 1179 |

The yield strength correlates with maximum round fiber count, round fiber trend angle and round fiber count average. The maximum number of round fiber count for samples 2, 7 and 9 are 1032, 1144 and 1489 respectively.

In the graph portrayed in figure 12 results also show for samples 7 and 2 a relatively constant circular fiber count all the way to the fracture plane in the 0.50-1.00 circularity bracket Sample 9 is an outlier though and has an increasing number of round fibers towards the fracture plane. The elliptical fiber count is also showing a growing trend-line toward the fracture plane on all the samples, although the count is way lower.

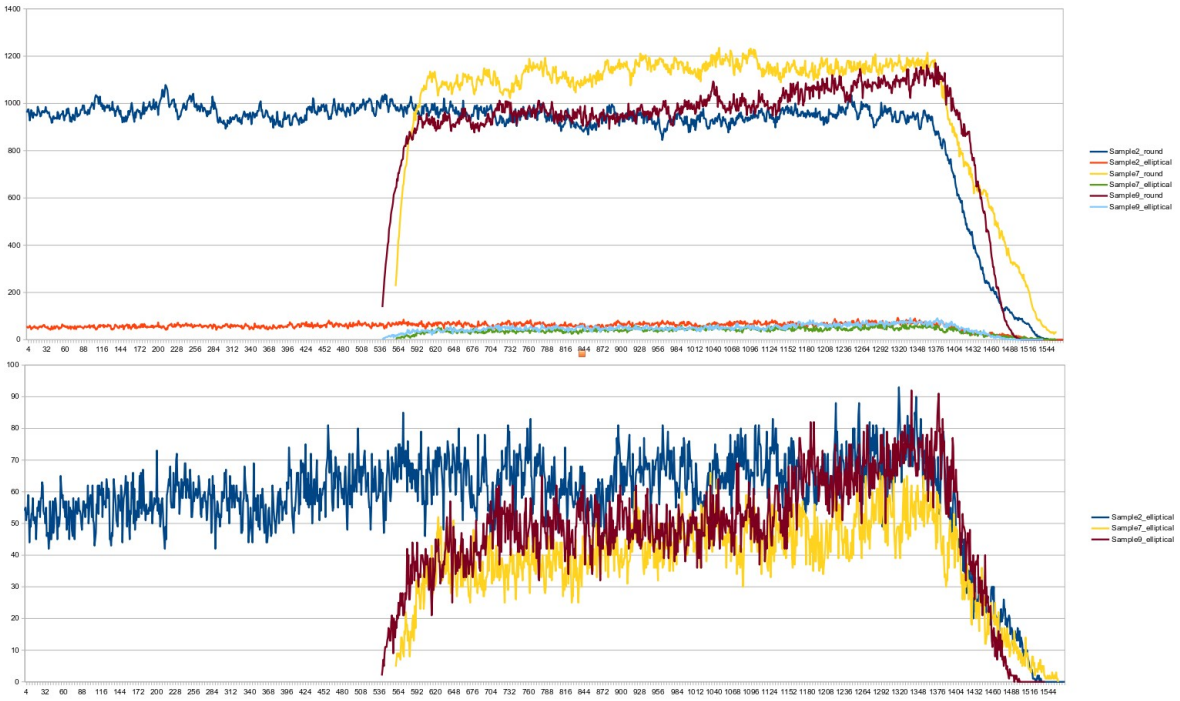


Figure 12. Graphs for 0.00-0.50 and 0.50-1.00 roundness.

The 0.96 roundness divided data in table 3 still shows a growing trendline for the elliptical fibers, and total fibers and the elliptical fiber count as lower than the round fiber count. The count trendline toward the fracture plane increases on sample 9, slightly increases on sample 7 and actually decreases on sample 2.

In table 3 the results for the count for 0.00-0.96 and 0.96-1.00 roundness divided values show very little correlation with tensile strength. Only the total fiber count trendline toward fracture plane correlates slightly with tensile strength.

Table 3. Analysis results for 0.00-0.96 and 0.96-1.00 roundness.

| SAMPLE | SAMPLE 2 | SAMPLE 7 | SAMPLE 9 |
|---|---|---|---|
| YIELD STRENGTH (MPa) | 24.299 | 24.569 | 24.913 |
| (MIN)MAX FIBER COUNT ROUNDNESS 0.96-1 | (530)783 | (701)897 | (509)669 |
| (MIN)MAX FIBER COUNT ELLIPTICAL 0.00-0.96 | (329)514 | (307)496 | (332)662 |
| ROUND FIBER TREND LINE ANGLE | -0.037 | 0.169 | 0.051 |
| ELLIPTICAL FIBER TREND LINE ANGLE TOWARD FRACTURE PLANE | 0.024 | 0.113 | 0.334 |
| TOTAL FIBER COUNT TREND LINE TOWARD FRACTURE PLANE | -0.012 | 0.130 | 0.28 |
| FIBER COUNT AVERAGE | 1017 | 1181 | 1048 |
| FRACTURE PLANE TRENDLINE | -6.617 | -6.487 | -10.837 |

From the graph in figure 13 we can see this in practice. Especially sample 9 has an increasing trendline toward the fracture plane for elliptical fibers, reaching up to same count as round fibers.

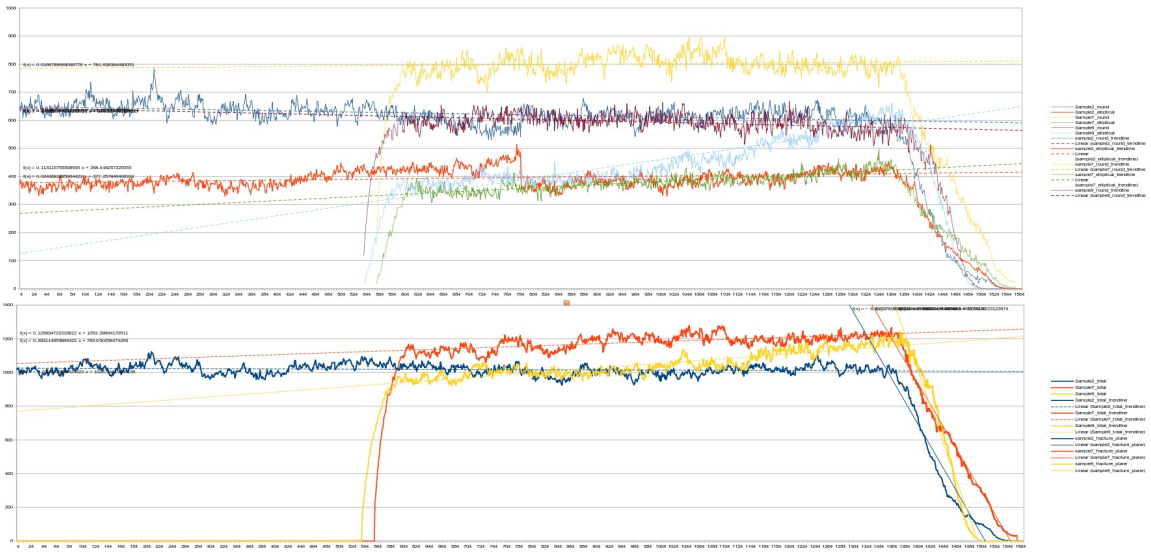

Figure 13. Graph for 0.00-0.96 and 0.96-1.00 roundness.

The graph also shows an interesting anomaly between layers 700-800 for sample two elliptical and round fiber count. An almost perpendicular incline down for the elliptical count and an equally steep step up for the round count.

## 3.2 Fiber area data

Table 4 shows how the trendline for samples 2 and 7 have an increasing trendline of area per layer towards the fracture plane and sample 9 has a decreasing trendline. It also shows how the fracture plane trendline is steeper the more stronger the composite sample was.

Table 4. Analysis results for 0.00-0.96 and 0.96-1.00 area.

| SAMPLE | SAMPLE 2 | SAMPLE 7 | SAMPLE 9 |
|---|---|---|---|
| YIELD STRENGTH (MPa) | 24.299 | 24.569 | 24.913 |
| (MIN)MAX FIBER AREA | (15102)21450 | (10442)15861 | (11294)15414 |
| TOTAL AREA FIBER TREND LINE | 1.45 | 3.29 | -1.01 |
| ROUND FIBER AREA TREND LINE | -0.037 | 0.169 | 0.051 |
| ANGLE TOWARD FRACTURE PLANE | -0.012 | 0.130 | 0.283 |
| ROUND FIBER AREA AVERAGE | 18007 | 13007 | 13291 |
| FRACTURE PLANE TRENDLINE | -81 | -101 | -116 |

The total area of fiber per layer plotted in figure 14 pretty closely stays the same along the samples, but a slight positive increase toward the fracture plane can be seen in sample 7 and 2. When dividing areas by roundness, we can see differences. In roundness 0.96-1.00 samples 7 and 9 the area increases toward the fracture planes. In sample 7 the elliptical areas also increase toward the fracture plane. Samples 9 and 2 have a decreasing area for roundness values of 0.96-1.00.

Average fiber area until fracture plane start is highest in sample 2, but lowest in sample 7. Samples 2 and seven both show a sudden peak in elliptical fiber area at the beginning of the fracture plane.

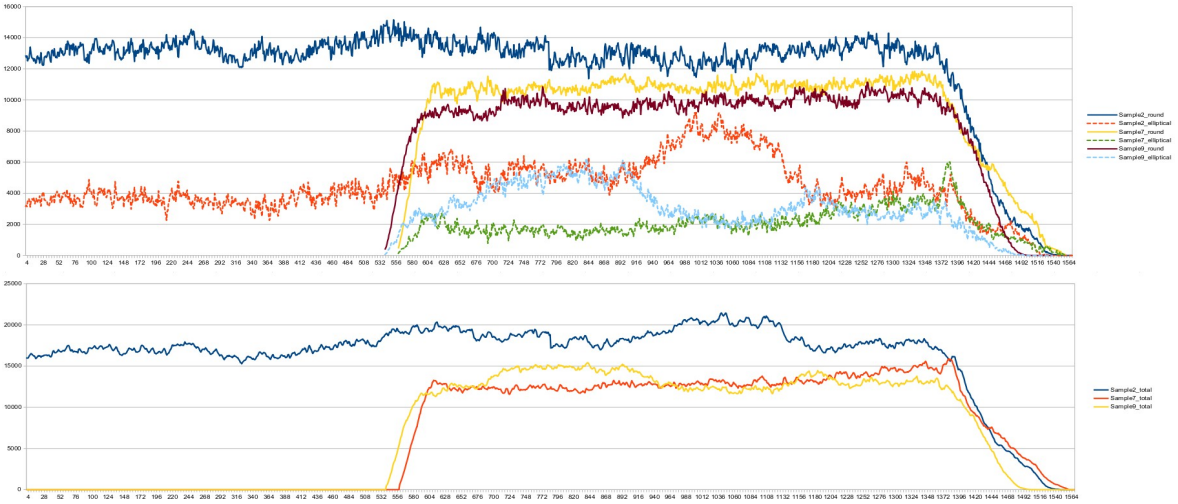

Figure 14. Graph of fiber area per layer.

The elliptical fiber peak area has a peak near the fracture area in both samples 2 and 7, which were also the weakest samples. This would indicate some sort of an anomaly at the fracture surface.

## 3.3 Average fiber size data

The average fiber/fiber bundle size data shows a slight increase towards the fracture plane on samples 2 and 7, but a decrease in sample 9. Both samples 2 and 7 have a peak increase of the average fiber size in the fracture area, especially sample 2.

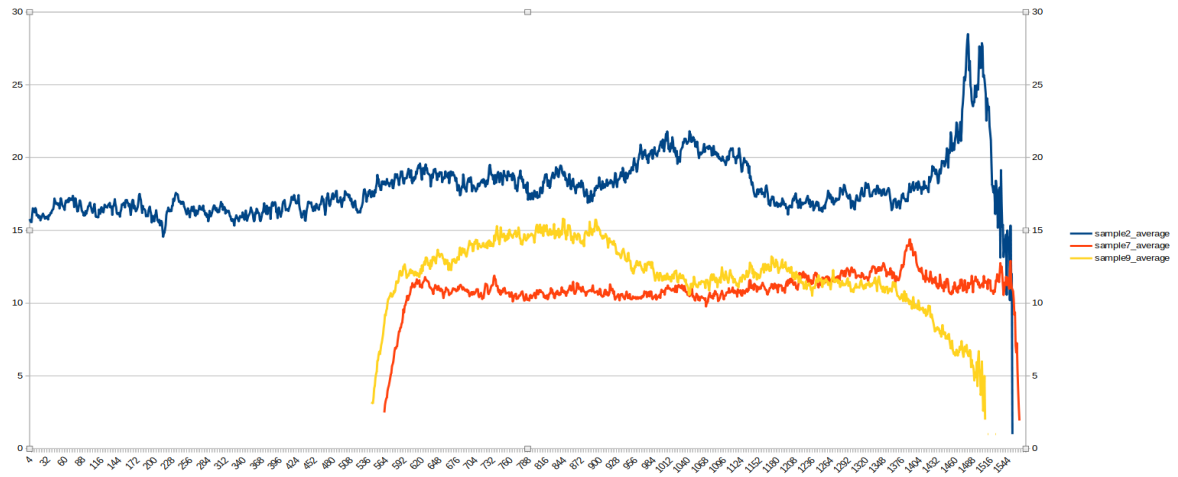


Figure 15. Graph of average area of fiber/bundle.

Although small, sample 7 has its fiber bundle on the left side of the fracture in the graph, showing a small peak in average area. Sample 2 has its fiber bundle relatively close to the end, showing a very large increase in average area.

## 3.4 Visual inspection

As seen in figures 16 and 17 taken from the coincident plane of the tensile strength test and sample extrusion to mold, visual inspection shows that both samples 7 (figure 16) and 2 (figure 17) had fiber bundles in the fracture plane, especially sample 2 which had a very large bundle in the corner. It's suspected that the fracture began propagation from these anomalies. It is noteworthy that these bundles are aligned relatively perpendicular to the tensile strength test.

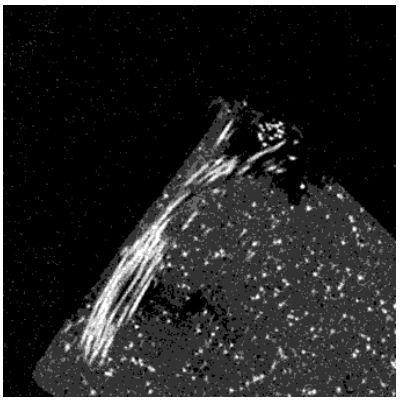

Figure 16. View of sample 2 fiber bundle anomaly.

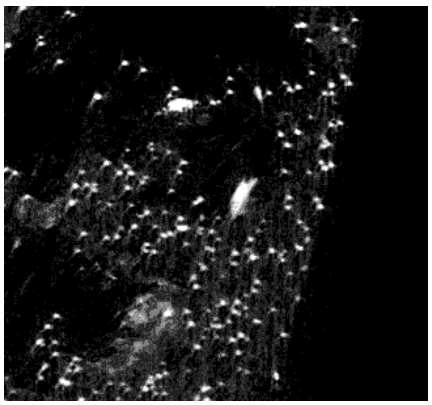

Figure 17. View of sample 7 fiber bundle anomaly.

Such anomalies are scattered around the samples, showing inconsistency in the fiber-matrix mixture. Sample 2s fracture had the largest of these anomalies however, which is consistent with its lowest tensile strength and sample 9 didn't have any significant anomalies in the fracture surface, again consistent with its highest tensile strength.

Another visual cue from the images is how most of the fibers are oriented parallel to the mold injection direction in all of the samples, as can be seen in figure 18, where the right – left is the tensile test axis.

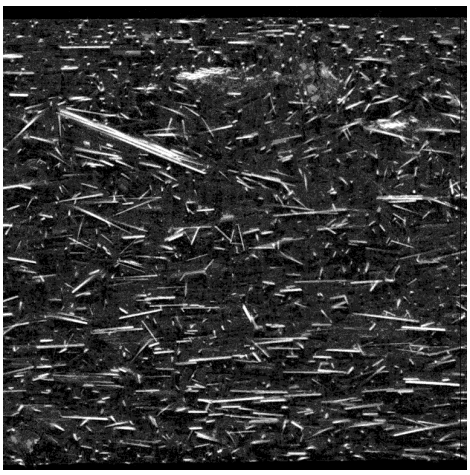

Figure 18. Right - Left tensile test axis showing fiber orientation.

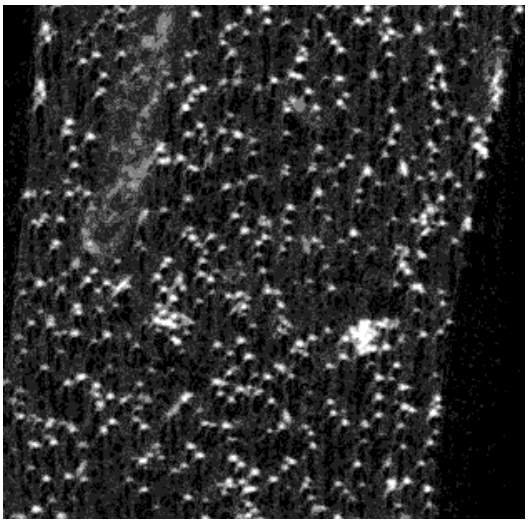

Figure 19. Coincident to tensile test axis showing fiber orientation.

When it is compared to figure 19 with plane coincident to tensile test axis, it can be clearly seen how fiber orientation is along the tensile test axis.

Although visual inspection as a method is rudimentary at best, it still shows clearly that the orientation is indeed along the tensile test axis. It also looks like fiber-pullout is the primary method of failure in these samples as can be interpreted from the spiky failure plane shown in figure 20.

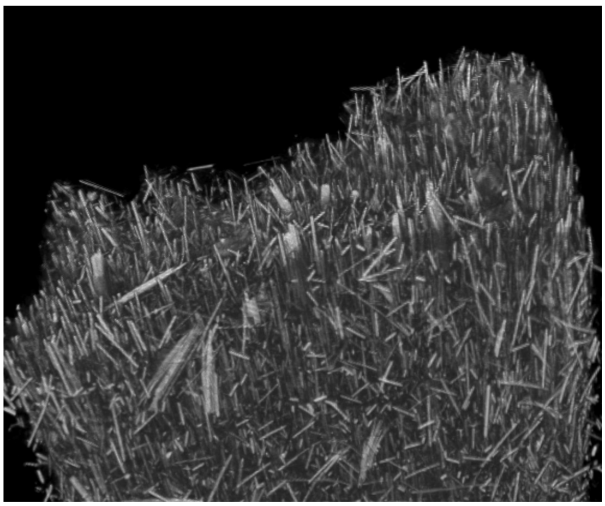

Figure 20. Spiky surface showing fiber pull-outs.

The failure plane also shows some cavities prior to arriving at the failure plane, which could indicate fiber pull-out to the other side. It’s however very inconclusive and hard to make out from the low contrast between matrix and void, and CT shadows.

# 4 Discussion

The results from both numerical and visual inspection of the samples show a key finding that injection molding of small fiber composite parts does not create a truly isotropic material. In general randomly oriented FRC have been called isotropic materials in literature, but at least according to the results it is false and they should be considered anisotropic. Fibers are aligned along the material injector because of the shear stresses and elongation at extrusion point, creating an anisotropic material as predicted by Vahid Monfared (2020, 923). Research in to changing the injection parameters to lessen the injector acclimatization of the fibers could be made, and in to how it affects the strength of the part. In some cases realignment of the mold can be done to improve the directional strength of the part. Hypothetically the tensile strength should be significantly weaker on off-axis of the material, as predicted by analytical and numerical calculations in literature (Cox 195;, Blumentritt et al. 1974; Halpin & Kardos 1976; Hu X. et al. 2016; Huang et al. 2019). In some applications, like extrusion formed composite beams and structures like the ones manufactured at Lappeenranta University of Technology, this is probably a good thing, as off-axis tensile forces are uncommon.

The results also show the injection mold cavity fills with irregular amounts of fiber, with the fiber amount either growing or decreasing as the cavity is being filled. Because of the small sample size of only the same size samples in this study and the variable imaging methods, it's impossible to tell if this effect is lessened or increased with a larger cavity, variable injection rates or even temperatures of the injected composite. It is also impossible to tell if the effect is only local variation, and a larger image would provide different results. Hypothetically the cause for this could be because the pressured difference between the inside of the extruding part of the injector changes as the cavity fills, changing the elongation of the composite mass or fluid propagation in the cavity. FE-modelling and empiric testing could be done to inspect the phenomenon.

An interesting peculiarity is that the failure point of the composite is often located at the end of the sample with the highest fiber count. This is opposite of what is expected, since composite tensile strength tends to increases with more fiber until a critical volume, as noted in literature (Meyers & Chawla 2010, 780-783; Pramudia, Khoirul, & Prihantoko

2022, 2). However the actual volume of the fibers stays relatively same, leading to the conclusion that the fibers either grow in size or become bundled, this is further elaborated later on. This increase in fiber count can be also affected by the method of imaging or post-processing of the images. For example in samples 7 and 9 it can be clearly seen, that the image contrast at the beginning of the voxel imaging isn't high enough to even properly detect the fibers. It quickly improves though, and seems relatively stable after the first 40 or so images, which were omitted from the analysis. The average fiber area for the total of the sample, and therefore volume slightly correlates with the tensile strength of the samples. However the volume calculations from the images need to consider fiber count and area of samples 7 and 9 isn't comparable to sample 2, which had different imaging parameters but ignoring sample 2, sample 9's higher average fiber area correlates with it's higher tensile strength.

Sample 9 and sample 7 also showed differences in the fracture plane angle in both fiber area and count, where sample 9 has clearly a more perpendicular fracture. Sample 2 falls in between, but since it has the highest fiber area because of the contrast difference, it can't be compared directly. It's also difficult to use the post-processing to level out the differences, since there is no base point to rely on. Basing the post processing to the known volumetric quantity of the fiber could work, but the accuracy is dependent on the accuracy of the equal material distribution in the parts from the injected material.

Looking at the elliptical count and area the amount of fibers aligned perpendicular to x-axis is increasing towards the fracture plane, which means it could have a negative effect on the tensile strength along x-axis. Especially the data from 0.00-0.50 roundness shows this, as the amount increases on all samples toward the fracture plane. This is supported by the research made by Hanhan et al. (2020) and Xiaofang Hu et al. (2016), as fibers aligned perpendicular to x-axis increase the amount of hydrostatic stress concentrations within the matrix. The average size of a fiber in a cross-section of the sample and visual inspection of the samples shows that diametrically larger fibers and bundles of fibers could lower the tensile stress, affirming what is seen in literature (Moon et al. 1992, 446; Thomason 2008, 1623). This is because fiber-fiber interface is weaker than matrix-fiber or matrix-matrix interface, and bundled fibers cause higher stress concentrations in the matrix. Attenuating the fiber load bearing force further, the shear-strength reliant surface area of a fiber grows linearly with fiber diameter assuming the length stays the same, but fiber strength grows

quadratically. The area tensile strength at the end of a fiber does also grow quadratically, but the tensile strength of fiber-matrix interface is much lower than the shear strength of the same interface. This leads to the tip nucleation and pull-out of the fibers, instead of fiber breakage as the failure mode. This can be hypothesized by the following equations, that demonstrate the status required for fiber breakage, instead of pull-out:

$$\sigma_{maxi} A_{\sigma} + A_{\tau} \tau_{maxi} > A_{\sigma} \sigma_{maxf} \tag{17}$$

$$\rightarrow \sigma_{maxi} + \frac{A_{\tau} \tau_{maxi}}{A_{\sigma}} > \sigma_{maxf} \tag{18}$$

where:

$$A_{\sigma} = \pi r^2 \tag{19}$$

and:

$$A_{\tau} = 2 \pi l \tag{20}$$

Equation 17 is derived from simple mechanical principles and physical dimensions shown in figure 17. It shows how the maximum forces acting on a fiber before failure. Pull-out or fiber breakage can be illustrated with the maximum tensile stress in the interface between the face of the fiber and the maximum shear stress in the curved surface of the fiber. In equation 17 $\sigma_{maxi}$ is the maximum tensile strength of the fiber-matrix interface (MPa), $\tau_{maxi}$ is the maximum shear strength of the fiber-matrix interface (MPa), and $\sigma_{maxf}$ is the maximum tensile strength of the fiber (MPa), with $A_{\tau}$ and $A_{\sigma}$ representing the area of shear stress and area of tensile stress ($mm^2$), respectively. Since:

$$\frac{A_\tau \tau_{maxi}}{A_\sigma} \tag{21}$$

decreases quadratically as the radius of the fiber increases, the end of the fiber has to carry proportionally higher loads. By increasing the length of the fiber with the diameter keeping the aspect ratio the same, thicker fibers can be used without losing strength. This is also supported in more detail by experimental, analytical and numerical analysis in literature. (Moon et al. 1992, 447; Huang et al. 2019, 6; Zhong, Liu, Pei, Sorkin, Louis, Commillus, Su, Guo, Thitsartarn, Lin, He & Zhang 2020, 7-9; Patel & Jain 2021, 4.)

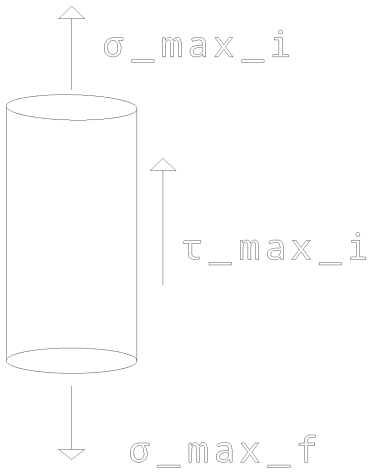


Figure 21. Stresses acting on a fiber.

Samples 2 and 7 had bundled fibers that probably were critical in causing the failure of the material. These bundles can be seen in figures 17. and 16. Hypothetically a method for quantifying fiber bundling from 3D-images could be derived to determine the Weibull modulus for randomly oriented short FRCs. The way used in this research paper with simple particle analysis of the average single fiber areas from 2D-layers has its caveats. It doesn't recognize thicker fibers and the fiber area increased by the perpendicularity to the image layer. You can analyze using only elliptical fibers, but as the ellipticity of the fiber grows so does its area, regardless of it's thickness or bundling. A method for quantifying

the Weibull modulus from the used materials would also be useful in parts that have rigid strength demands, like automotive parts.

In visual inspection figures 19. and 20. show fiber pull-outs that have happened in the fracture plane, which would according to literature predict smaller fiber aspect ratios, meaning thicker and shorter fibers, or bundling of the fibers. Fiber property data, like average aspect ratio and standard deviation could be compared to these findings if we had it.

# 5 Conclusions

A simple numerical 3 dimensional layered analysis is performed to inspect the fracture mechanics and behaviour of GFRP by means of open software. Although the objectives of the research weren't achieved, some findings on composites were made. The greatest key finding was that these randomly oriented FRCs are in fact not randomly oriented. Injector acclimatizes the fibers parallel to the axis of injection, making randomly oriented FRCs an anisotropic material. I hypothesize this has significant effects on the off-axis strength of the material and should be accounted for in calculations especially for mission-critical components. However a sample size of 3 is too low to make any conclusions on possible strength predictions, but the some results align with established results in literature and some align against it. It's established that bundled fibers cause weak points for crack propagation as we saw in this research. Some results did go against the current literature, for example the samples didn't usually break where the area or fiber count and area was lowest, but towards where the fiber count and area increased, even though in literature most randomly-oriented fiber composites increase in tensile strength up to a critical point of 50% or higher fiber volume. No easily calculable properties that would precisely predict the material tensile strength or behaviour during failure were found. More research on the subject is needed, especially a larger sample size and imaging of the failure-areas before and maybe even during the tensile stress test. More rigid imaging parameters and pre-processing would be also improve results, to make the samples more comparable. A study to inspect the accuracy of multiple other orientation algorithms would provide valuable insight in to the accuracy of this method. Especially an algorithm by Eekhoff and Lake from 2020 originally for imaging of fibrous biological tissue looks promising in analysing such scenarios. However that was out of the scope of this project. An algorithm or some sort of numerical analysis that could determine fiber pull-out ratio to fiber breakage in the material could also be developed, to inspect the effect of volumetric fiber quantity and fiber properties like aspect ratio to the percentage of the pull-out and fiber breakage.

It was shown that CT images from commercially available machines usually used for electronics inspection can be used for numerical analysis of complicated and even low-density, low difference in attenuation coefficient materials, with open source software

available to everyone. Relatively simple-to-use methods are available, but their caveat is processing power requirements for such large sample sizes, which requires either breaking down samples to smaller sections, using smaller samples, or using computers for data processing with high amounts of working memory.

# References

Abhay Shivanagere, S.K. & Goyal, S.P. 2018. Modelling of Glass fiber Reinforced Polymer (GFRP) for Aerospace Applications. Journal of Engineering Science and Technology, 13: 11. Pp. 3710-3728.

Affdl, J.C.H. & Kardos, J.L. 1976. The halpin-tsai equations: a review. Polymer Engineering & Science, 16: 5, Pp. 344–352.

Agyei, R., Hanhan, I. & Sangid, M.D. 2023. A data-driven microstructural rationale for micro-void nucleation in discontinuous fiber composites. Journal of Thermoplastic Composite Materials, 36: 4. Pp. 1694–1716.

Behera, S., Mohanty, J.R., Nath, G. & Mahanta, T.K. 2023. Exploring properties of short randomly oriented rattan fiber reinforced epoxy composite for automotive application. Journal of Natural Fibers, 20: 1. Pp. 1-13.

Bhat, A.R., Kumar, R. & Mural, P.K.S. 2023. Natural fiber reinforced polymer composites: A comprehensive review of Tribo-Mechanical properties. Tribology International, 189. Pp. 1-29.

Blumentritt, B.F., Vu, B.T. & Cooper, S.L. 1974. The mechanical properties of oriented discontinuous fiber-reinforced thermoplastics. I. Unidirectional fiber orientation. Polymer Engineering & Science, 14: 9. Pp. 633–640.

Brunke, O., Brockdorf, K., Drews, S., Müller, B., Donath, T., Herzen, J. & Beckmann, F. 2008. Comparison between x-ray tube-based and synchrotron radiation-based μCT. Proceedings of the 2008 symposium of Optical Engineering + Applications. San Diego, California, USA. 10-14.8.2008. San Diego, California, USA: Proceedings Volume 7078, Developments in X-Ray Tomography VI. P. 1-12

Chow, T.S. 1977. Elastic moduli of filled polymers: The effect of particle shape. Journal of Applied Physics, 48: 10. Pp. 4072–4075.

Cox, H.L. 1952. The elasticity and strength of paper and other fibrous materials. British Journal of Applied Physics, 3: 3. Pp. 72–79.

Eekhoff, J.D. & Lake, S.P. .2020. Three-dimensional computation of fibre orientation, diameter and branching in segmented image stacks of fibrous networks. Journal of The Royal Society Interface, 17: 169. Pp. 1-14.

Eshelby, J.D. 1957. The determination of the elastic field of an ellipsoidal inclusion, and related problems. Proceedings of the Royal Society of London. Series A. Mathematical and Physical Sciences, 241: 1226. Pp. 376–396.

Essabir, H., Bouhfid, R. & Qaiss, A. 2017. [Chapter 8:] Alfa and doum fiber-based composite materials for different applications. In: Jawaid, M., Tahir, P.M., & Saba, N. Lignocellulosic Fibre and Biomass-Based Composite Materials. Elsevier. Pp. 147–164.

Faruk, O., Bledzki, A.K., Fink, H.-P. & Sain, M. 2014. Progress report on natural fiber reinforced composites: progress report on natural fiber composites. Macromolecular Materials and Engineering, 299: 1. Pp. 9–26.

Fu, S.-Y. & Lauke, B. 1998. The elastic modulus of misaligned short-fiber-reinforced polymers. Composites Science and Technology, 58: 3–4. Pp. 389–400.

Fu, S.-Y., Yue, C.-Y., Hu, X. & Mai, Y.-W. 2000. On the elastic stress transfer and longitudinal modulus of unidirectional multi-short-fiber composites. Composites Science and Technology, 60: 16. Pp. 3001–3012.

Gao, Y., Hu, W., Xin, S. & Sun, L. 2022. A review of applications of CT imaging on fiber reinforced composites. Journal of Composite Materials, 56: 1. Pp. 133–164.

Garcea, S.C., Wang, Y. & Withers, P.J. 2018. X-ray computed tomography of polymer composites. Composites Science and Technology, 156. Pp. 305–319.

Goh, K.L., Aspden, R.M. & Hukins, D.W.L. 2004. Review: finite element analysis of stress transfer in short-fibre composite materials. Composites Science and Technology, 64: 9. Pp. 1091–1100.

Gusev, A.A. 2017. Finite element estimates of viscoelastic stiffness of short glass fiber reinforced composites. Composite Structures, 171. Pp. 53–62.

Hanhan, I., Agyei, R.F., Xiao, X. & Sangid, M.D. 2020. Predicting microstructural void nucleation in discontinuous fiber composites through coupled in-situ x-ray tomography experiments and simulations. Scientific Reports, 10: 1. Pp. 1-8.

Hashimoto, M., Okabe, T., Sasayama, T., Matsutani, H. & Nishikawa, M. 2012. Prediction of tensile strength of discontinuous carbon fiber/polypropylene composite with fiber orientation distribution. Composites Part A: Applied Science and Manufacturing, 43: 10. Pp. 1791–1799.

Hsueh, C.-H. 1990. Interfacial debonding and fiber pull-out stresses of fiber-reinforced composites. Materials Science and Engineering: A, 123: 1. Pp. 1–11.

Hu, X., Fang, J., Xu, F., Dong, B., Xiao, Y. & Wang, L. 2016. Real internal microstructure based key mechanism analysis on the micro-damage process of short fibre-reinforced composites. Scientific Reports, 6: 1. Pp. 1-9.

Hu, X.F., Chen, B.Y., Tirvaudey, M., Tan, V.B.C. & Tay, T.E. 2016. Integrated XFEM-CE analysis of delamination migration in multi-directional composite laminates. Composites Part A: Applied Science and Manufacturing, 90. Pp. 161–173.

Huang, Z.-M., Zhang, C.-C. & Xue, Y.-D. 2019. Stiffness prediction of short fiber reinforced composites. International Journal of Mechanical Sciences, 161–162. Pp. 1-14.

Junaedi, H., Baig, M., Dawood, A., Albahkali, E. & Almajid, A. 2021. Modeling analysis of the tensile strength of polypropylene base Short Carbon Fiber reinforced composites. Journal of Materials Research and Technology, 11. Pp. 1611–1621.

Kagawa, H., Umezu, Y., Sakaue, K. & Koyanagi, J. 2023. Numerical simulation for the tensile failure of randomly oriented short fiber reinforced plastics based on a viscoelastic entropy damage criterion. Composites Part C: Open Access, 10. Pp. 1-7.

Kalasova, D., Brinek, A., Slouf, M., Duskova-Smrckova, M., Zikmund, T., Patakova, Z. & Kaiser, J. 2020. Wide-cone angle phase-contrast x-ray computed tomography of synthetic polymer materials. IEEE Transactions on Instrumentation and Measurement, 69: 11. Pp. 8910–8918.

Karakoç, A., Miettinen, A., Virkajärvi, J. & Joffe, R. 2021. Effective elastic properties of biocomposites using 3D computational homogenization and X-ray microcomputed tomography. Composite Structures, 273. Pp. 1-10

Kivelä, Simo K. 1989 Algebra ja geometria. Espoo: Otatieto. 201 p.

Koyanagi, J., Kawamoto, K., Higuchi, R., Tan, V.B.C. & Tay, T.-E. 2021. Direct FE2 for simulating strain-rate dependent compressive failure of cylindrical CFRP. Composites Part C: Open Access, 5. Pp. 1-8.

Margaritondo, G. & Hwu, Y. 2021. Imaging with coherent x-rays: from the early synchrotron tests to synapse. Journal of Imaging, 7: 8. Pp. 1-32.

Mertens, J.C.E., Williams, J.J. & Chawla, N. 2014. Development of a lab-scale, high-resolution, tube-generated X-ray computed-tomography system for three-dimensional (3D) materials characterization. Materials Characterization, 92. Pp. 36–48.

Meyers, M.A. & Chawla, K.K. 2010. Mechanical behavior of materials. 2. ed., 4. print. with corr. Cambridge: Cambridge University Press. 851 p.

Mirkhalaf, M., Eggels, E., Thoopul, A.A., Larsson, F. & Fagerström, M. 2019. Short fiber composites: Computational homogenization vs orientation averaging. Proceedings of the 22nd International Conference on Composite Materials. Melbourne, Australia. 11-16.8.2019. P. 1-8.

Monfared, V. 2020 [Chapter 31:] Problems in short-fiber composites and analysis of chopped fiber-reinforced materials. In: Samui, Pijush, Kim, Dookie, Iyer, R., Nagesh & Chaudhary Sandeep. New Materials in Civil Engineering. Elsevier, Pp. 919–1043.

Moon, C.K., Lee, J., Cho, H.H. & Kim, K.S. 1992. Effect of diameter and surface treatment of fiber on interfacial shear strength in glass fiber/epoxy and HDPE. Journal of Applied Polymer Science, 45: 3. Pp. 443–450.

Mori, T. & Tanaka, K. 1973. Average stress in matrix and average elastic energy of materials with misfitting inclusions. Acta Metallurgica, 21: 5. Pp. 571–574.

Pan, N. 1996. The elastic constants of randomly oriented fiber composites: a new approach to prediction. Science and Engineering of Composite Materials, 5: 2. Pp. 1-10.

Pan, Y., Iorga, L. & Pelegri, A.A. 2008. Analysis of 3D random chopped fiber reinforced composites using FEM and random sequential adsorption. Computational Materials Science, 43: 3. Pp. 450–461.

Patel, N. & Jain, P. 2021. An investigation on mechanical properties in randomly oriented short natural fiber reinforced composites. Materials Today: Proceedings, 37. Pp. 469–479.

Piggott, M.R. 1980. Load-bearing fibre composites. 1st ed. Oxford New York: Pergamon Press. 277 p.

Pramudia, M., Khoirul Umami, M. & Prihantoko, A. 2022. Effect of fiber volume fraction on tensile strength and fracture analysis of corn husk reinforced epoxy resin composite. MATEC Web of Conferences 372. Pp. 1-4

Putra, I.S., Budiman, B.A., Sambegoro, P.L., Santosa, S.P., Mahyuddin, A.I., Kishimoto, K. & Inaba, K. 2020. The influence of fiber surface profile and roughness to fiber–matrix interfacial properties. Journal of Composite Materials, 54: 11. Pp. 1441–1452.

Reddy, S. & Mandava, R. 2013. Aero Space Applications of GFRP Composites: Review. [web document]. Guntur: 2013 [Referred 17,1,2025]. Review. R.V.R. & J.C. College of Engineering. 4 p. Available in PDF-file: https://www.researchgate.net/publication/259568833.

Sankur, B. 2004. Survey over image thresholding techniques and quantitative performance evaluation. Journal of Electronic Imaging, 13: 1. Pp. 146-166.

Sato, M., Hasegawa, K., Koyanagi, J., Higuchi, R. & Ishida, Y. 2021. Residual strength prediction for unidirectional CFRP using a nonlinear viscoelastic constitutive equation considering entropy damage. Composites Part A: Applied Science and Manufacturing, 141. Pp. 1-8.

Scott, A.E., Hepples, W., Kalantzis, N., Wright, P., Mavrogordato, M.N., Sinclair, I. & Spearing, S.M. 2011. High resolution damage detection of loaded carbon/epoxy laminates using synchrotron radiation computed tomography' Proceedings of the 18th International Conference on Composite Materials.. ICC Jeju, Korea. P. 1–6

Scott, A.E., Sinclair, I., Spearing, S.M., Mavrogordato, M.N. & Hepples, W. 2014. Influence of voids on damage mechanisms in carbon/epoxy composites determined via high resolution computed tomography. Composites Science and Technology, 90. Pp. 147–153.

Shokrian, M.D., Shelesh-Nezhad, K. & Soudmand, B.H. 2016. 3D FE analysis of tensile behavior for co-PP/SGF composite by considering interfacial debonding using CZM. Journal of Reinforced Plastics and Composites, 35: 5. Pp. 365–374.

Sokac, M., Santosi, Z., Vukelic, D., Katic, M., Durakbasa, N.M. & Budak, I. 2021. Geometric tolerancing analysis of multi-material components (MMCs) obtained by industrial x-ray computed tomography. In: N.M. Durakbasa & M.G. Gençyılmaz (eds) Digital Conversion on the Way to Industry 4.0. Cham: Springer International Publishing, Pp. 607–613.

Stock, S.R. 2008. Recent advances in X-ray microtomography applied to materials. International Materials Reviews, 53: 3. Pp. 129–181.

Tay, T.E., Liu, G., Tan, V.B.C., Sun, X.S. & Pham, D.C. 2008. Progressive failure analysis of composites. Journal of Composite Materials, 42: 18. Pp. 1921–1966.

Thomason, J.L. 2008. The influence of fibre length, diameter and concentration on the strength and strain to failure of glass fibre-reinforced polyamide 6,6. Composites Part A: Applied Science and Manufacturing, 39: 10. Pp. 1618–1624.

Verho, T., Fortino, S., Hradil, P., Turpeinen, T., Immonen, K., Harlin, A. & Sandquist, D. 2022. Biocomposite modeling by tomographic feature extraction and synthetic microstructure reconstruction. Composites Science and Technology, 230. Pp. 1-9.

Vijayakumar, S. & Palanikumar, K. 2020. Evaluation on mechanical properties of randomly oriented Caryota fiber reinforced polymer composites. Journal of Materials Research and Technology, 9: 4. Pp. 7915–7925.

Villarino, M.B. 2005. Ramanujan’s perimeter of an ellipse [web document]. San José: February 2008 [Referred 17.1.2025]. Escuela de Matemática, Universidad de Costa Rica. 12 p. Available in PDF-file: https://arxiv.org/pdf/math/0506384v1.

Wang, Y., Mikkelsen, L.P., Pyka, G. & Withers, P.J. 2018. Time-lapse helical x-ray computed tomography (Ct) study of tensile fatigue damage formation in composites for wind turbine blades. Materials, 11: 11. Pp. 1-11.

Williams, J.G. 1990. Fracture mechanics of composites failure. Proceedings of the Institution of Mechanical Engineers, Part C: Mechanical Engineering Science, 204: 4. Pp. 209–218.

Yen, J-.C., Chang, F.-J., & Chang S. 1995. A new criterion for automatic multilevel thresholding. IEEE Transactions on Image Processing, 4: 3. Pp. 370–378.

Zhandarov, S. & Mäder, E. 2005. Characterization of fiber/matrix interface strength: applicability of different tests, approaches and parameters. Composites Science and Technology, 65: 1. Pp. 149–160.

Zhang, P., Feng, Y., Bui, T.Q., Hu, X. & Yao, W. 2020. Modelling distinct failure mechanisms in composite materials by a combined phase field method. Composite Structures, 232. Pp. 1-13.

Zhong, Y., Liu, P., Pei, Q., Sorkin, V., Louis Commillus, A., Su, Z., Guo, T., Thitsartarn, W., Lin, T., He, C. & Zhang, Y.-W. 2020. Elastic properties of injection molded short glass fiber reinforced thermoplastic composites. Composite Structures, 254. Pp. 1-11.

Zwanenburg, E.A., Norman, D.G., Qian, C., Kendall, K.N., Williams, M.A. & Warnett, J.M. 2023. Effective X-ray micro computed tomography imaging of carbon fibre composites. Composites Part B: Engineering, 258. Pp. 1-10.